Accurate Spin-Orbit Coupling and Intersystem Crossing by Relativistic Mixed-Reference Spin-Flip (MRSF)-TDDFT

Konstantin Komarov,[†] Woojin Park,[‡] Seunghoon Lee,[*,¶] Tao Zeng,[*,§] and Cheol Ho Choi[*,‡]

†*Center for Quantum Dynamics, Pohang University of Science and Technology, Pohang 37673, South Korea*

‡*Department of Chemistry, Kyungpook National University, Daegu 41566, South Korea*

¶*Division of Chemistry and Chemical Engineering, California Institute of Technology, Pasadena, California 91125, USA*

§*Department of Chemistry, York University, Toronto, ON M3J 1P3, Canada*

E-mail: slee89@caltech.edu; tzeng@yorku.ca; cchoi@knu.ac.kr

Abstract

Relativistic MRSF-TDDFT is developed considering the spin-orbit coupling (SOC) within the mean-field approximation. The resulting SOC-MRSF faithfully reproduces the experiments with very high accuracy, which is also consistent with the values by four-component (4c) relativistic CASSCF and 4c-CASPT2 in the spin-orbit-energy splitting calculations of the C, Si and Ge atoms. Even for the fifth-row element Sn, the SOC-MRSF yielded accurate splittings ($\sim$ 3 % error). In the SOC calculations of the molecular 4-thiothymine with a third-row element, SOC-MRSF values are in excellent agreement with those of SO-GMC-QDPT2 level, regardless of geometries and exchange-correlation functionals. The same SOC-MRSF predicted the anticipated chance of S_1 ($n\pi^*$) $\longrightarrow$ T_1 ($\pi\pi^*$) intersystem crossing, even in thymine with only second-row elements. With its accuracy and practicality, thus, SOC-MRSF is a promising electronic structure protocol in challenging situations such as nonadiabatic molecular dynamics (NAMD) incorporating both internal conversions and intersystem crossings in large systems.

TOC Graphic

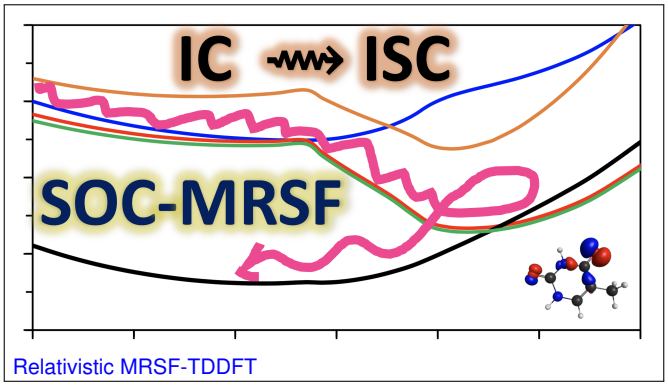

Keywords

MRSF-TDDFT, NAMD, Relativistic Effect, Spin-Orbit Coupling, Intersystem Crossing

Introduction

The interest in intersystem crossings (ISC) or spin crossovers has been intensified by the advent of femtosecond time-resolved spectroscopic studies showing that ISC may occur at the picosecond timescale. In the case of xanthone,[1] the $^1n\pi^* \longrightarrow {}^3\pi\pi^*$ ISC takes place within $\sim$ 2.0 ps right after an ultrafast $^1\pi\pi^* \longrightarrow {}^1n\pi^*$ internal conversion (IC). Wolf et al.[2] have also obtained a circumstantial experimental evidence of the population transfer to triplet states on the timescale of 3.5$\pm$0.3 ps in the photo-dynamics of thymine. El-Sayed's rule forbids ISC between singlet and triplet (doublet and quartet, triplet and quintet, etc.) states with the same occupation scheme. For instance, the $^1\pi\pi^* \leftrightarrow {}^3\pi\pi^*$ and $^1n\pi^* \leftrightarrow {}^3n\pi^*$ conversions are forbidden due to the lack of orientational changes of spatial orbitals. As implied above, therefore, same-configuration ISCs must involve the cooperation of IC and ISC, e.g., $^3\pi\pi^* \xrightarrow{IC} {}^3n\pi^* \xrightarrow{ISC} {}^1\pi\pi^*$, emphasizing the importance of treating IC and ISC on the equal footing in many dynamical processes involving spin-flipping.[3,4]

In addition, recent experimental advances of X–ray spectroscopy also require accurate computational methods with the proper spin-orbit couplings (SOC) to account for the spectra of heavy element compounds.[5] The ISC plays a major role in the phenomenon of thermally activated delayed fluorescence (TADF)[6] as well, in which the triplet-to-singlet ISC facilitates the harvesting of the triplet excitons in organic light-emitting diodes (OLEDs). As the typical system size of TADF materials increases, efficient quantum chemistry methods are highly desirable for the computations of SOCs among various excited states.

Regarding excited state dynamics, its non-adiabatic dynamical nature of IC and ISC requires intensive computations of excited states' energies, wave functions, and overlaps of the wave functions at adjacent time steps. Proper descriptions of various excited states are also challenging due to their distinctively different characters. Considering these, it is necessary to perform theoretical simulations using a methodology that: (i) provides a balanced and accurate treatment of both dynamic correlation and non-dynamic correlation (e.g. including the important *double* excitations) of the electronic states; (ii) is capable of correctly describing the conical intersections (CI) between

ground and excited states as well as between different excited states; (iii) can provide efficient computations of both non-adiabatic and spin-orbit couplings; (iv) is efficient enough to perform statistical sampling for several picoseconds of large molecular systems. Perhaps, one of the most popular and practical electronic structure theories for *ab initio* NAMD is TDDFT,[7] although it produces topologically wrong CI_{10}.[8] Throughout this work, CI_{IJ} is used to denote the conical intersection between adiabatic states I and J. Also, it was recently shown that both CASSCF and TDDFT fail to describe the S_2-to-S_1 internal conversions (ICs) of s-*trans*-butadiene and s-*trans*-hexatriene via CI_{21},[9] which is due to the missing of either dynamic correlation or the doubly excited configurations. In contrast, the recently developed mixed-reference spin-flip time-dependent density functional theory (MRSF-TDDFT, MRSF for brevity)[10–12] properly described not only CI_{10}[8] but also CI_{21}s,[9] in satisfactory agreement with the results of EOMCC as well as multi-state many-body perturbation theory, such as XMS-CASPT2.

In MRSF, the electronic ground and excited states are obtained from the poles of a novel mixed reference (MR) within the linear response (LR) regime. With the help of a novel spinor-like transformation, a *hypothetical* single reference is constructed from the $M_S = \pm 1$ components of the restricted open-shell KS determinant, expanding its response space significantly. Consequently, it nearly eliminates the problematic spin-contamination pitfalls of SF-TDDFT.[13] It also considers the singlet ground state and other excited states on the same footing, which not only eliminates the general topological problem[8] of CI_{10} by TDDFT but also allows to study open-shell ground singlet states.[14] Furthermore, the one-electron spin-flip excitation from the mixed triplet reference includes the HOMO-to-LUMO *doubly* excited configuration, which is the main ingredient to properly account for the $2^1A_g^-$ dark states of s-*trans*-butadiene and s-*trans*-hexatriene.[9] *Thus, MRSF gives a balanced treatment of* dynamic and nondynamic electron correlations for both ground and excited states, with the convenience of single determinant orbital optimization. These advantages allow the MRSF to overcome the major limitations of the conventional TDDFT variants, while reliably reproducing the results of the more expensive multi-reference *ab initio* wave function theories.[9] In a series of studies,[8,12,14–22] it has been demonstrated that the MRSF approach can also

yield accurate nonadiabatic coupling matrix elements (NACMEs),[15,17] enabling reliable non-adiabatic molecular dynamics (NAMD) simulations,[22–24] a topologically correct description of conical intersections,[8,18,21] and accurate values of singlet–triplet gaps.[14,16] This method has also been successfully used in designing high-performance optoelectronic materials.[25–27]

Given the efficiency and accuracy of the MRSF for both ground and excited states, it is imperative to introduce spin-orbit coupling (SOC) functionality in this scheme for expanding its applicabilities to intersystem crossing (ISC), which is the main subject of the present work. In the following, the basic spin-orbit coupling formulations of MRSF and its applications in some real systems are presented in order.

Theoretical Details of Relativistic MRSF-TDDFT

The introduction of SOC to DFT theory has been done either by variational or perturbative approaches.[4] Although there have been significant efforts of implementing the relativistic full four-component (4c) Dirac–Kohn–Sham formalism such as the recent linear damped response (LD)-TDDFT,[28] the four-component relativistic Hamiltonian is impractical for large systems.[29,30] On the other hand, various transformation schemes, e.g., Pauli, Douglas-Kroll, elimination of small components, infinite-order two-component, etc., are available to reduce the relativistic Hamiltonian to a two-component (2c) form, which can be separated to a spin-independent ($\hat{H}_0$) and a spin-dependent part. ($\hat{H}_{\mathrm{SOC}}$)

$$\hat{H} = \hat{H}_0 + \hat{H}_{\mathrm{SOC}}. \tag{1}$$

The spin-independent term includes the conventional non-relativistic Hamiltonian and the scalar relativistic Hamiltonian, while the spin-dependent second term contains the spin-orbit coupling (SOC) operator.

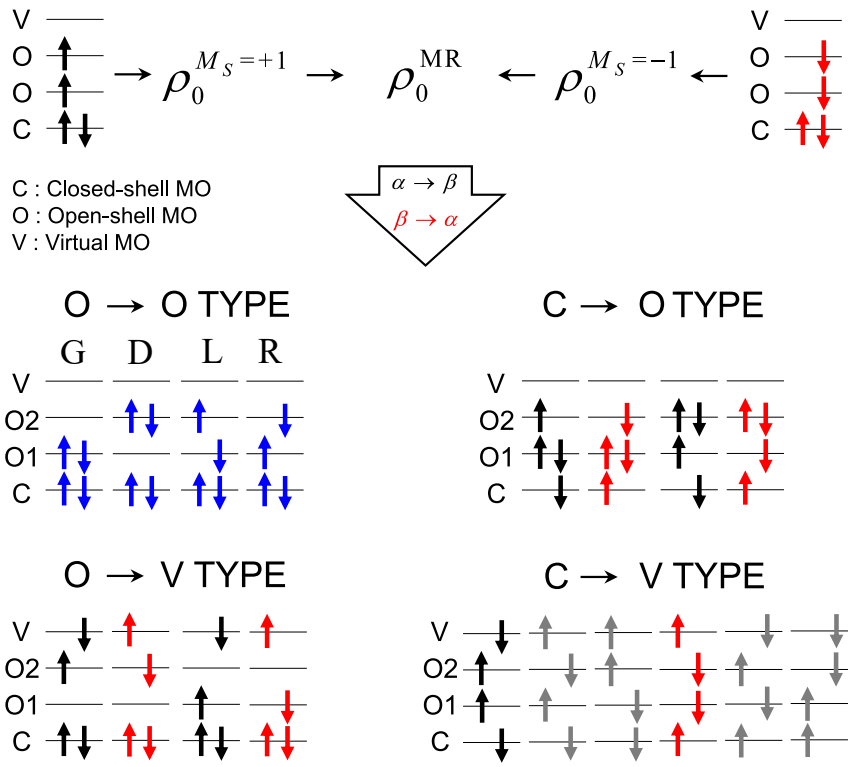

Figure 1: Electronic configurations of the $M_S = +1$ and $M_S = -1$ components of triplet reference in the upper panel and a complete set of configurations for MRSF-TDDFT in the lower panel. Response states are described by configurations represented with blue, black, and red arrows in MRSF-TDDFT. The configurations of red arrows are absent in SF-TDDFT.

Non-Relativistic and Relativistic States

In this work, we introduce the SOC effect in a perturbative manner. Accordingly, we solve the spin-independent Hamiltonian ($\hat{H}_0$) problem using the normal MRSF response calculations.[10,11] The resulting response states are constituting non-SOC singlet and triplet MRSF states with scalar relativistic corrections. With Casida's wavefunction ansatz,[31] they are labeled as $\Psi_I^{SM_S}$, where I denotes the I-th state in energy order within the manifold of total spin quantum number (S) and M_S indicates the total spin magnetic quantum number. The $\Psi_I^{SM_S}$ is given by a linear combination of configuration state functions (CSFs, $\Phi_{\mathrm{Type},k}^{SM_S}$) and broken symmetry configurations. (see Figure 1) There are three different "Type"s of CSFs originating from four types of single spin-flip (de-)excitation in MRSF abbreviated as OO, CO, OV and a broken symmetry "Type" CV. It should be emphasized that although all four OO, CO, OV, and CV contributions are utilized in the spin-independent

Hamiltonian problem including the scalar relativistic effect, the last CV-type is excluded in the evaluations of the SOC Hamiltonian matrix elements. This is because it breaks the time-reversal symmetry of SOC. Since the CV-types make minor contributions to the ground and low-lying excited states, they are not anticipated to be of importance for SOC values in those states. Without CV-types, the non-SOC MRSF wavefunction of the I-th electronic state of the singlet (Ψ_I^{00}) and the triplet with $M_S = 0$ (Ψ_I^{10}) can be represented as

$$|\Psi_I^{00}\rangle = X_{\mathrm{G}}^{00,I}|\Phi_{\mathrm{G}}^{00}\rangle + X_{\mathrm{D}}^{00,I}|\Phi_{\mathrm{D}}^{00}\rangle + X_{\mathrm{OO}}^{00,I}|\Phi_{\mathrm{OO}}^{00}\rangle + \sum_k X_{\mathrm{CO},k}^{00,I}|\Phi_{\mathrm{CO},k}^{00}\rangle + \sum_k X_{\mathrm{OV},k}^{00,I}|\Phi_{\mathrm{OV},k}^{00}\rangle, \quad (2)$$

$$|\Psi_I^{10}\rangle = X_{\mathrm{OO}}^{10,I}|\Phi_{\mathrm{OO}}^{10}\rangle + \sum_k X_{\mathrm{CO},k}^{10,I}|\Phi_{\mathrm{CO},k}^{10}\rangle + \sum_k X_{\mathrm{OV},k}^{10,I}|\Phi_{\mathrm{OV},k}^{10}\rangle, \quad (3)$$

respectively, where $X_{\mathrm{Type},k}^{SM_S}$ denotes amplitude of the CSF. As MRSF response calculations only generate $M_S = 0$ triplets, the rest $M_S = \pm 1$ triplets are obtained by applying the spin ladder operators ($\hat{S}_+, \hat{S}_-$) on the $M_S = 0$ components of the triplet states as

$$|\Psi_I^{11}\rangle = \frac{1}{\sqrt{2}}\hat{S}_+|\Psi_I^{10}\rangle, \quad (4)$$

$$|\Psi_I^{1\bar{1}}\rangle = \frac{1}{\sqrt{2}}\hat{S}_-|\Psi_I^{10}\rangle. \quad (5)$$

These non-SOC states then form a multi-electronic basis set in the construction of the SOC Hamiltonian matrix, i.e. $H_{IJ}^{SM_S S'M'_S} = \langle\Psi_I^{SM_S}|\hat{H}_0 + \hat{H}_{\mathrm{SOC}}|\Psi_J^{S'M'_S}\rangle$. Within the linear response formalism, the wavefunction introduced above is the eigenfunction of Casida's A matrix, which is different from the H_0 Hamiltonian matrix. To take it into account, we assume that the off-diagonal matrix elements for $\hat{H}_0$ are zero to be consistent with the rest of formulations, i.e. $\langle\Psi_I^{SM_S}|\hat{H}_0|\Psi_J^{S'M'_S}\rangle = E_I^S\delta_{IJ}\delta_{SS'}\delta_{M_S M'_S}$ where E_I^S is the total energy of MRSF non-SOC state. Accordingly, the final SOC states and their corresponding energies are obtained by diagonalizing the matrix, $H_{IJ}^{SM_S S'M'_S} = E_I^S\delta_{IJ}\delta_{SS'}\delta_{M_S M'_S} + \langle\Psi_I^{SM_S}|\hat{H}_{\mathrm{SOC}}|\Psi_J^{S'M'_S}\rangle$. The resulting SOC states (indexed by $\mathcal{J}$) are represented

as a linear combination of the non-SOC MRSF states:

$$|\Psi_{\mathcal{J}}\rangle = \sum_{S=0,1} \sum_{M_S=-S}^{S} \sum_{I} c_{\mathcal{J}I}^{SM_S} |\Psi_I^{SM_S}\rangle, \tag{6}$$

with the complex-valued coefficients $\left\{c_{\mathcal{J}I}^{SM_S}\right\}$.

Matrix Elements of $\hat{H}_{\mathrm{SOC}}$

To describe the matrix elements of $\hat{H}_{\mathrm{SOC}}$, it is convenient to adopt the historic Breit-Pauli (BP) operator, which is composed of one- and two-electron terms. Both terms arise from the interaction between electronic spin magnetic dipole and the magnetic fields generated by electronic rotation. The magnetic fields in the one- and two-electron terms stem from electronic rotation around nuclei and around other electrons, respectively.[32] Although the Breit-Pauli spin-orbit operator is adopted for demonstrating the SOC, the current implementation of SOC-MRSF accommodates other operators such as DK, RESC, and IOTC. The Breit-Pauli spin-orbit Hamiltonian is given by

$$\hat{H}_{\mathrm{SOC}} = \hat{H}_{\mathrm{en}} + \hat{H}_{\mathrm{ee}} = \frac{\alpha^2}{2} \sum_{aA} \frac{Z_A}{\hat{r}_{aA}^3} \hat{\mathbf{l}}_{aA} \cdot \hat{\mathbf{s}}_a - \frac{\alpha^2}{2} \sum_{a} \sum_{b \neq a} \frac{1}{\hat{r}_{ab}^3} \hat{\mathbf{l}}_{ab} \cdot (\hat{\mathbf{s}}_a + 2\hat{\mathbf{s}}_b) \tag{7}$$

where $\hat{\mathbf{l}}_{aA} = \hat{\mathbf{r}}_{aA} \times \hat{\mathbf{p}}_a$ is the angular momentum operator of the electron a relative to the nucleus A, and $\hat{\mathbf{l}}_{ab} = \hat{\mathbf{r}}_{ab} \times \hat{\mathbf{p}}_a$ is that relative to the electron b. The $\hat{\mathbf{r}}_a$, $\hat{\mathbf{p}}_a$, and $\hat{\mathbf{s}}_a$ are the position, momentum, and spin operators of the ath electron, and $\hat{r}_{ab} = |\hat{\mathbf{r}}_{ab}| = |\hat{\mathbf{r}}_a - \hat{\mathbf{r}}_b|$ and $\hat{r}_{aA} = |\hat{\mathbf{r}}_{aA}| = |\hat{\mathbf{r}}_a - \hat{\mathbf{R}}_A|$ are the distance between the electrons a and b and that between the electron a and the nucleus A, respectively.

The two-electron SOC is dominated by the interaction between core and valence electrons. Such a core-valence interaction reduces the nuclei-valence SOC. It can thus be treated as a mean-field screening of the one-electron SOC. In such a mean-field (MF) screening approximation,[33] the SOC becomes an effective one-electron operator, $\hat{H}_{\mathrm{SOMF}}$, with the following matrix element between

spin-orbital i and j of

$$\langle i|\hat{H}_{\mathrm{SOMF}}|j\rangle = \langle i|\hat{h}_{\mathrm{en}}|j\rangle + \sum_{kl} D_{kl}\left(\langle ik|\hat{h}_{\mathrm{ee}}|jl\rangle - \frac{3}{2}\langle ik|\hat{h}_{\mathrm{ee}}|lj\rangle - \frac{3}{2}\langle ki|\hat{h}_{\mathrm{ee}}|jl\rangle\right), \tag{8}$$

where D_{kl} is the single-particle density matrix element, which is approximated by the density of the restricted open-shell triplet reference state in this work. This is a reasonable choice, since most CSFs that contribute to low-lying states differ only by one-electron (de)excitation and spin-flip from the reference Kohn-Sham determinant within the space of the valence orbitals and the external unoccupied orbitals. Therefore, the core-valence screening of SOC is largely captured by using the reference density matrix.

In the second quantization formalism, the SOMF Hamiltonian can be rewritten as

$$\hat{H}_{\mathrm{SOMF}} = \sum_{ij}(V_{ij}^{x}\hat{T}_{ij}^{x} + V_{ij}^{y}\hat{T}_{ij}^{y} + V_{ij}^{z}\hat{T}_{ij}^{z}), \tag{9}$$

with the effective one-electron integrals ($V_{ij}^{x,y,z}$)

$$\mathbf{V}_{ij} = \langle i|\hat{\mathbf{h}}_{\mathrm{en}}|j\rangle + \sum_{kl} D_{kl}\left(\langle ik|\hat{\mathbf{h}}_{\mathrm{ee}}|jl\rangle - \frac{3}{2}\langle ik|\hat{\mathbf{h}}_{\mathrm{ee}}|lj\rangle - \frac{3}{2}\langle ki|\hat{\mathbf{h}}_{\mathrm{ee}}|jl\rangle\right), \tag{10}$$

$$\hat{\mathbf{h}}_{\mathrm{en}} = \frac{\alpha^2}{2}\sum_{A}\frac{Z_A}{\hat{r}_{1A}^3}\hat{\mathbf{l}}_{1A}, \;\; \hat{\mathbf{h}}_{\mathrm{ee}} = -\frac{\alpha^2}{2}\frac{1}{\hat{r}_{12}^3}\hat{\mathbf{l}}_{12}, \tag{11}$$

and the Cartesian triplet operators ($\hat{T}_{ij}^{x,y,z}$)

$$\hat{T}_{ij}^{x} = \frac{1}{2}(\hat{a}_{i\alpha}^{\dagger}\hat{a}_{j\beta} + \hat{a}_{i\beta}^{\dagger}\hat{a}_{j\alpha}), \tag{12}$$

$$\hat{T}_{ij}^{y} = \frac{1}{2i}(\hat{a}_{i\alpha}^{\dagger}\hat{a}_{j\beta} - \hat{a}_{i\beta}^{\dagger}\hat{a}_{j\alpha}), \tag{13}$$

$$\hat{T}_{ij}^{z} = \frac{1}{2}(\hat{a}_{i\alpha}^{\dagger}\hat{a}_{j\alpha} - \hat{a}_{i\beta}^{\dagger}\hat{a}_{j\beta}). \tag{14}$$

Note that i and j here index spatial MOs, instead of spin orbitals, and the transition operators are introduced in Cartesian form for convenient representation. The Cartesian and spherical forms of

triplet operators connected by the following linear transformation:

$$\begin{pmatrix} \hat{T}^x \\ \hat{T}^y \\ \hat{T}^z \end{pmatrix} = \begin{pmatrix} -\frac{1}{2} & -\frac{1}{2i} & 0 \\ \frac{1}{2} & -\frac{1}{2i} & 0 \\ 0 & 0 & \frac{1}{\sqrt{2}} \end{pmatrix} \begin{pmatrix} \hat{T}^{1,1} \\ \hat{T}^{1,-1} \\ \hat{T}^{1,0} \end{pmatrix}. \tag{15}$$

Spin-Dependent Transition Density Matrix

To incorporate the $\langle i|\hat{H}_{\mathrm{SOMF}}|j\rangle$ effective one-electron SOC matrix elements between spin orbitals into the SOC matrix elements between MRSF multi-electronic states, the one-electron spin-dependent transition density matrices between the MRSF states need to be constructed. Their elements adopt the forms of:

$$D_{ij}^{IJ}(1,1) = \langle \Psi_I^{SM_S}|\hat{T}^{1,1}|\Psi_J^{S'M'_S}\rangle \delta_{M_S,M'_S+1}, \tag{16}$$

$$D_{ij}^{IJ}(1,-1) = \langle \Psi_I^{SM_S}|\hat{T}^{1,-1}|\Psi_J^{S'M'_S}\rangle \delta_{M_S,M'_S-1}, \tag{17}$$

$$D_{ij}^{IJ}(1,0) = \langle \Psi_I^{SM_S}|\hat{T}^{1,0}|\Psi_J^{S'M'_S}\rangle \delta_{M_S,M'_S}. \tag{18}$$

Explicit expressions of the density matrices were obtained (see SI for detailed forms) by using the python-based SecondQuantizationAlgebra library[34,35] and Wick's theorem.[36] Finally, the matrix elements of the SOMF Hamiltonian can be obtained by the contraction of the transformed density matrices with the effective one-electron integrals in Eq. 10. The complex-valued Hermitian matrix is then diagonalized to give eigenvalues and eigenstates of the SOC-included Hamiltonian operator.

Time-reversal Symmetry for Transition Density Matrix

Using the relations from the time reversal symmetry,

$$\hat{\mathcal{T}}\hat{a}_{p\alpha}^\dagger\hat{\mathcal{T}}^{-1} = \hat{a}_{p\beta}^\dagger, \quad \hat{\mathcal{T}}\hat{a}_{p\beta}^\dagger\hat{\mathcal{T}}^{-1} = -\hat{a}_{p\alpha}^\dagger, \quad \hat{\mathcal{T}}\hat{a}_{q\alpha}\hat{\mathcal{T}}^{-1} = \hat{a}_{q\beta}, \quad \hat{\mathcal{T}}\hat{a}_{q\beta}\hat{\mathcal{T}}^{-1} = -\hat{a}_{q\alpha}, \tag{19}$$

$$\hat{\mathcal{T}}|S,M_S\rangle = (-1)^{S-M_S}|S,-M_S\rangle, \quad \hat{\mathcal{T}}^{-1}|S,M_S\rangle = (-1)^{S+M_S}|S,-M_S\rangle\rangle, \tag{20}$$

14 relations can be deduced as summarized in supporting information, which we can reduce the effort to compute the spin-dependent transition density matrices. For example, we can find an equality between two different transition density matrices

$$\langle \Psi_I^{00} | a_{p\beta}^\dagger a_{q\beta} | \Psi_J^{00} \rangle = \langle \Psi_I^{00} | \hat{\mathcal{T}} a_{p\alpha}^\dagger \hat{\mathcal{T}}^{-1} \hat{\mathcal{T}} a_{q\alpha} \hat{\mathcal{T}}^{-1} | \Psi_J^{00} \rangle = \langle \Psi_I^{00} | a_{p\alpha}^\dagger a_{q\alpha} | \Psi_J^{00} \rangle. \tag{21}$$

or

$$\begin{aligned} \langle \Psi_I^{00} | a_{p\beta}^\dagger a_{q\alpha} | \Psi_J^{11} \rangle &= \frac{1}{\sqrt{2}} \langle \Psi_I^{00} | a_{p\beta}^\dagger a_{q\alpha} \hat{S}_+ | \Psi_J^{10} \rangle = \frac{1}{\sqrt{2}} \langle \Psi_I^{00} | a_{p\beta}^\dagger a_{q\beta} | \Psi_J^{10} \rangle + \frac{1}{\sqrt{2}} \langle \Psi_I^{00} | a_{p\beta}^\dagger \hat{S}_+ a_{q\alpha} | \Psi_J^{10} \rangle \\ &= \frac{1}{\sqrt{2}} \langle \Psi_I^{00} | \hat{\mathcal{T}} a_{p\alpha}^\dagger \hat{\mathcal{T}}^{-1} \hat{\mathcal{T}} a_{q\alpha} \hat{\mathcal{T}}^{-1} | \Psi_J^{10} \rangle - \frac{1}{\sqrt{2}} \langle \Psi_I^{00} | a_{p\alpha}^\dagger a_{q\alpha} | \Psi_J^{10} \rangle = -\sqrt{2} \langle \Psi_I^{00} | a_{p\alpha}^\dagger a_{q\alpha} | \Psi_J^{10} \rangle, \end{aligned} \tag{22}$$

with Eq. (4) and the commutation relations: $[\hat{S}_+, a_{q\alpha}] = -a_{q\beta}$ and $[\hat{S}_+, a_{p\beta}^\dagger] = a_{p\alpha}^\dagger$. Other examples are also listed in Supporting Information.

Results and Discussions

In order to carefully analyze the accuracy of the relativistic MRSF-TDDFT (SOC-MRSF), the SOC-corrected energy levels of C, Si, Ge and Sn atoms were considered, since both accurate high-level calculations and experimental data of those atoms are available. Following these atomic systems, SOC-MRSF was applied to the real molecular systems of 4-thiothymine, which has a third-row element of Sulfur. Finally, the chance of the intersystem crossing (ISC) in thymine was investigated.

$^3P_1 - ^3P_0$ Gap of Group 14 Elements

Without SOC, the Group 14 elements (C, Si, Ge and Sn) have a 3-fold spin degeneracy and a 3-fold spatial degeneracy in their ^3P ground state. The degeneracy is lifted by the SOC, resulting in the $^3P_0$, $^3P_1$, and $^3P_2$ levels. The energy gap between the lowest $^3P_0$ ground state and the first excited

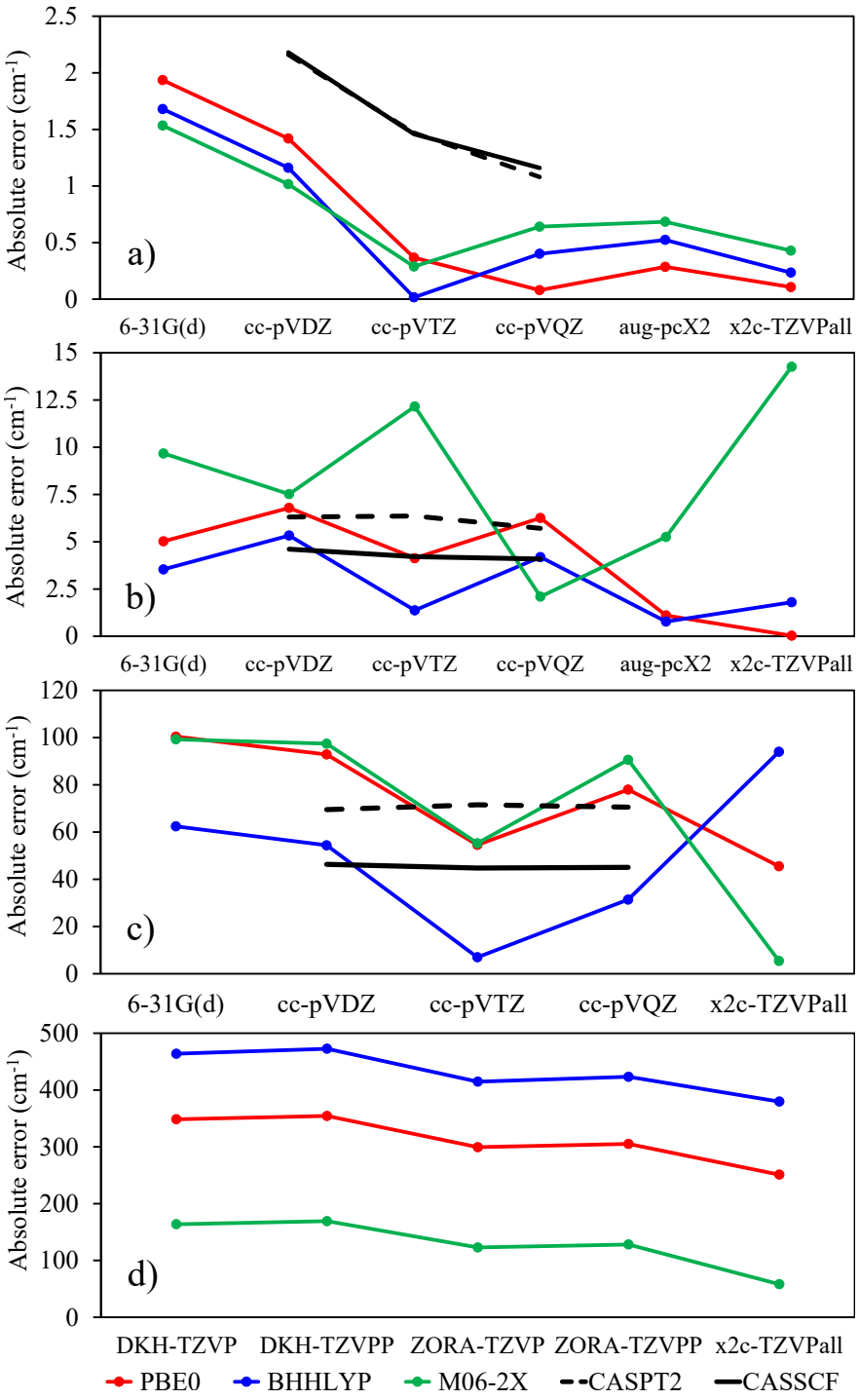

Figure 2: Absolute spin-orbit splitting errors ($^3P_1 - ^3P_0$ Gap in cm^{-1}) of (a) C, (b) Si, (c) Ge and (d) Sn as compared to the experimental values. The PBE0 (red), BH&HLYP (blue) and M06-2X (green) functionals were adopted for SOC-MRSF. For comparison, the results of 4c-CASPT2 (dotted) and 4c-CASSCF (solid black line) using uncontracted cc-pVXZ (X = D, T, Q)[37] were also shown.

$^3P_1$ state can be a good measure of relativistic effects. The absolute errors in the gaps as compared to experimental data as well as previous high-level fully relativistic four-component (4c-) CASSCF and 4c-CASPT2 calculations[37] are presented in Fig. 2. The experimental $^3P_1$ - $^3P_0$ splittings are 16.4 cm^{-1} (C),[38] 77.1 cm^{-1} (Si),[39] 557.1 cm^{-1} (Ge),[40] and 1691.8 cm^{-1} (Sn).[41]

The three different exchange-correlation (XC) functionals of PBE0, BH&HLYP and M06-2X were adopted in combination with various basis sets. For all calculations, the Douglas-Kroll (DK) second-order transformation was utilized for the scalar relativistic effect. In the case of C, the error decreases with larger basis sets, showing the importance of basis set. On the other hand, the XC functional dependencies are relatively smaller. Interestingly, the combination of BH&HLYP/cc-pVTZ yields a value with near zero error. In the case of Si, while the errors of both PBE0 and BH&HLYP functionals are generally small and insensitive to the basis sets, those of M06-2X show quite strong basis set dependencies. As in the case of C, the BH&HLYP/cc-pVTZ combination gives the smallest error. For the heavier element of Ge, BH&HLYP functional performs well and gives errors similar to those of 4c-CASSCF and 4c-CASPT2. It is interesting to see that the particular combination of BH&HLYP/cc-pVTZ consistently yielded a near-perfect prediction even in Ge. The better performance of BH&HLYP than the other functionals can be attributed to the formulation of MRSF. As was pointed out by Huix-Rotllant et al.,[42] within the widely used collinear (one-component) SF formalism, the configurations obtained by different SF transitions couple through the exact exchange only. As the current implementation of MRSF utilizes the same collinear formalism, it requires a larger fraction of the exact exchange, such as in the BHHLYP functional.

In the case of the heaviest fifth-row element Sn, the accuracy of the M06-2X functional appears to be much better than BH&HLYP. Due to its strong SOC, the adoption of x2x-TZVPall basis sets has a high impact, yielding an excellent accuracy with $\sim 3\%$ error. However, the good agreement of Sn can be due to an error cancellation. A source of error in our SOC-MRSF scheme comes from the perturbative SOC treatment, which is limited to the L-S coupling for all these atoms. While such a coupling scheme works well for light-weighted elements, it fails to describe heavy elements

with much stronger SOC. The alternative j-j coupling is more appropriate in those cases. For such a situation, SOC needs to be included in the orbital optimization step, generating spinors that mix α and β spin functions. This non-perturbative SOC scheme requires two-component atomic orbitals as basis sets and is beyond our current SOC-MRSF scheme. Nonetheless, it is quite remarkable that the overall accuracy with less than 10% error is achieved by our SOC-MRSF-TDDFT up to the fifth row in the periodic table. And the SOC-MRSF splittings compare favorably with the 4c-CASSCF and 4c-CASPT2 results.

Table 1: The predicted $^3P_1 - ^3P_0$ gaps (and prediction errors in %) of C, Si, Ge and Sn in cm^{-1} by SOC-MRSF/PBE0 with the effective core potential of SBJKC. The effective nuclear charges (ENC) are adopted.

	C	Si	Ge	Sn
SOC-MRSF/SBKJC/PBE0	16.5 (1%)	75.7 (-2%)	587.6 (5%)	2051.5 (21%)
ENC[43]	3.9	168	1312	5500

Relativistic quantum chemistry calculations for heavy element compounds often employ effective core potentials (ECP). Without the core electrons and orbitals, the core-valence two-electron SOC screening can be described using effective nuclear charges (ENC). The SBKJC ECP and its associated ENCs were used with SOC-MRSF to calculate the $^3P_1$-$^3P_0$ gaps of the Group 14 elements from C to Sn, and the results are listed in Table 1, along with the ENC values. The PBE0 functional was utilized in the calculations. Only one-electron contribution is included in the SOC calculations and Pauli-Breit 1st order relativistic corrections were applied to it. This is because the ENCs were devised based on this combination. Using the ENC developed by Koseki et al.[44,45] , excellent agreements with experiments are seen from the results of C, Si and Ge atoms (less than 5% errors). In the case of the heavier element Sn, the error is increased to 21%.

Table 2: The predicted $^3P_1 - ^3P_0$ gap (its errors in %) of Sn in cm^{-1} with various all-electron scalar relativity treatments.

	DK			IOTC	RESC
	1st	2nd	3rd		
M06-2X/x2c-TZVPall	1757 (4%)	1750 (3%)	1750 (3%)	1750 (3%)	1861 (10%)

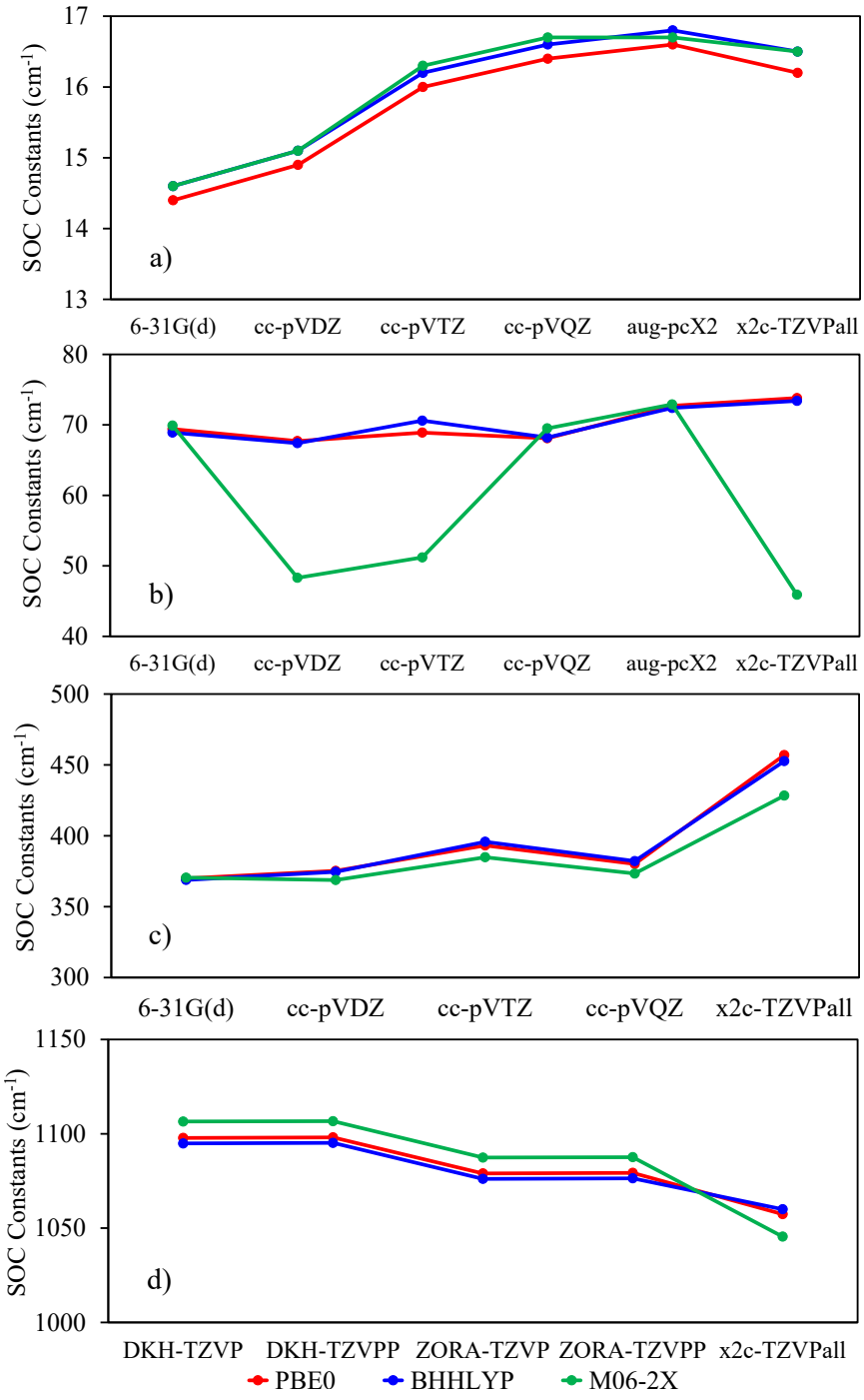

Figure 3: The calculated spin-orbit coupling constants in cm^{-1} between lowest singlet and lowest triplet states of (a) C, (b) Si, (c) Ge and (d) Sn. The PBE0 (red), BH&HLYP (blue) and M06-2X (green) functionals were adopted for SOC-MRSF. In the case of Sn, various speicalized basis sets are utilized.

The effect of different scalar relativistic schemes on the SOC-MRSF results was investigated on the fifth-row element Sn and the results are presented in Table 2. Since the scalar relativistic effects are included during the orbital optimization process, in principle it can have a profound effect on the final relativistic energies. Although it is mostly due to error cancellations, the prediction by M06-2X functional in combination with the x2c-TZVPall basis set is quite accurate for Sn in Fig. 2(d). Therefore, SOC-MRSF calculations were performed with M06-2X/x2c-TZVPall for the investigations. Although the higher order Douglas-Kroll (DK) transformation generally improves the accuracy, the order has little effect on the Sn $^3P_0$-$^3P_1$ gap. While the IOTC (infinite-order two-component method)[46] shows a similar small 3% error, the RESC (relativistic elimination of small component)[47] transformation somewhat deteriorates the agreement. Since the aforementioned error cancellation is still valid, it would be a good practice to check the particular combination of functional, basis sets, and scalar relativistic transformation against available experimental atomic spectra, especially for the heavy atoms, before applying SOC-MRSF. Ovrall, the SOC-MRSF with BH&HLYP/cc-pVTZ appears to be a magic choice upto fourth-row elements, while M06-2X/x2c-TZVPall can produce good results for fifth-row ones.

The SOC constants between the lowest triplet (^3P) and lowest singlet states (^1D) of C, Si, Ge and Sn obtained by SOC-MRSF are presented in Fig. 3. The corresponding experimental SOC couplings of C and Si are 13.98 and 73.70 cm^{-1}.[48,49] The calculated SOC constants are generally insensitive to the choice of XC functionals, while it is gradually affected by the size of basis sets. In terms of absolute values, the SOC constants of C and Si are calculated with < 15% errors.

Spin-Orbit Couplings of 4-Thiothymine

As a representative third-row system, 4-thiothymine is adopted for SOC-MRSF to validate its SOC predictions.[50–56] The lowest singlet excited state (S_1) has a $^1n\pi^*$ character with the sulfur lone pair orbitals, which is nearly degenerate with the two lowest triplet $^3n\pi^*$ and $^3\pi\pi^*$ states at the S_1 minimum geometry. Depending on the exchange-correlation functionals for TDDFT and CASPT2 methods, it was reported that the $^1n\pi^*$ can be either S_1 or S_2. Although they are nearly degenerate,

the $^3\pi\pi^*$ and $^3n\pi^*$ are T_1 and T_2, respectively, showing that the corresponding states are sensitive to the choice of theories.[57]

To explore functional dependencies, the B3LYP, PBE0, BH&HLYP and M06-2X functionals were utilized in the current SOC-MRSF calculations. Furthermore, in order to study the geometric effects, the S_1 minimum geometry was first individually optimized with the respective exchange-correlation functionals by MRSF-TDDFT/6-31G*. SOC-MRSF/cc-pVTZ calculations were then performed at the optimized geometries.

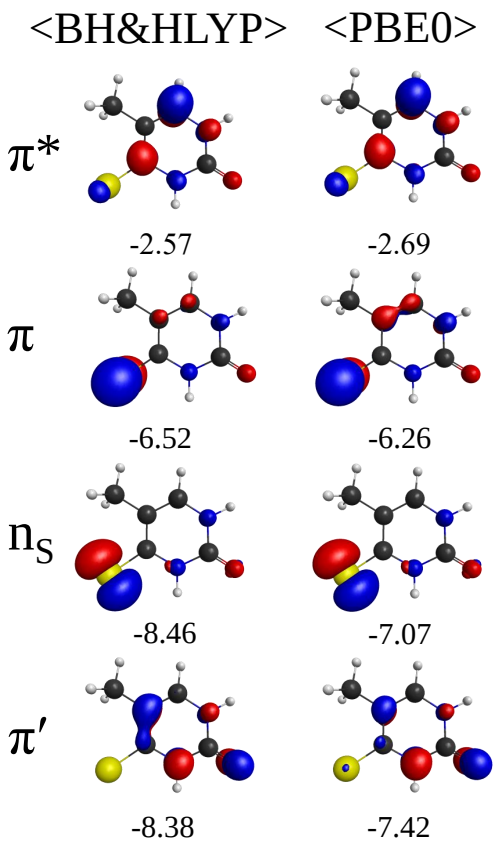

Figure 4: ROHF molecular orbitals and their energies in eV of 4-Thiothymine at $S_{1\ min}$ geometry by MRSF/cc-pVTZ with BH&HLYP and PBE0 functionals. The geometries of each functionals are taken from Fig. S1. The character of S_0, S_1, T_1, and T_3 states with squared transition coefficients are given in bottom.

As reference values, the single point SOC calculations by the SO-GMC-QDPT2[58]/cc-pVTZ level were also performed at the S_1 minimum geometry optimized by the MRSF/6-31G* with four different functionals. The optimized S_1 geometries of 4-thiothymine by B3LYP, PBE0, BH&HLYP and M06-2X functionals are shown in Figure S1. While the optimized geometries of B3LYP, PBE0 and BH&HLYP agree within ~ 0.03 Å with each other, the bond lengths of the M06-2X-optimized structure are generally longer by ~ 0.1 Å. Using these, the vertical excitation energies (VEEs) of both non-SOC and SOC (*italic*) states as calculated by various theories and the results are presented in Table S1. The GMC-QDPT2 results indicate that regardless of reference geometry, the relative state order is $^3n\pi^*$ < $^3\pi\pi^*$ < $^1n\pi^*$. Except for M06-2X, the $^3n\pi^*$ by MRSF is slightly lower than $^3\pi\pi^*$. However, unlike GMC-QDPT2, the relative state order of $^1n\pi^*$ is in between the two triplet states according to B3LYP, BH&HLYP and PBE0. In general, as seen in previous studies,[57] the three states are nearly degenerate with each other and their relative orders are sensitive to the choice of theories.

Using the same methodologies, the spin-orbit coupling (SOC) values of 4-thiothymine were calculated by SOC-MRSF-TDDFT as well as GMC-QDPT2 and the results are shown in Table 3. The SOC values of S_0(GS)/$^3n\pi^*$, S_0(GS)/$^3\pi\pi^*$, $^1n\pi^*$/$^3n\pi^*$, and $^1n\pi^*$/$^3\pi\pi^*$ were investigated. It is noted that the one- and two-electron contributions to the overall SOCs are separately listed. As expected by the El-Sayed's rule, the SOCs of GS/$^3n\pi^*$ and $^1n\pi^*$/$^3\pi\pi^*$ have sizable values of 98/13 and 113/14 cm^{-1} in the case of GMC-QDPT2 at PBE0 geometry, indicating that the SOC of S/T($M_s = \pm 1$) (the former value of /) are much bigger than that of S/T($M_s = 0$) (the latter value of /). This is because we chose a coordinate frame such that the $\Delta M_S = \pm 1$ SOC arises from the electron rotation of an in-plane orbital (e.g., the n orbital) to an out-of-plane orbital (e.g., the π and π^* orbitals). As anticipated, the $1e$ contribution is much bigger than $2e$. The SOC values of GMC-QDPT2/cc-pVTZ are relatively insensitive to the geometric effects. Regardless of exchange-correlation functionals, SOC-MRSF values are in excellent agreement with the SO-GMC-QDPT2 references. The SOC values of GS/$^3\pi\pi^*$ and $^1n\pi^*$/$^3n\pi^*$ are negligibly small as it should be. The reference ROHF orbitals by BH&HLYP and PBE0 functionals are shown

Table 3: Spin-orbit couplings of 4-thiothymine (in cm^{-1}) computed by SOC-MRSF-TDDFT and GMC-QDPT2 with cc-pVTZ basis set at S_{1min} geometries optimized by MRSF/6-31G* with respective functional. The double slash (//) is utilized to emphasize the correspondingly optimized geometries. The values with $M_s = \pm 1$ and $M_s = 0$ triplets are separated by slash symbol. The 1e and 2e components as well as the combined values are separately shown.

		1e		2e		1e+2e		
		Real	Imag	Real	Imag	Real	Imag	Abs.
MRSF/PBE0	GS/$^3\pi\pi^*$	0/0	0/-1	0/0	0/1	0/0	0/0	0/0
	GS/$^3n\pi^*$	15/0	-102/11	-4/0	21/-2	11/0	-81/9	82/9
	$^1n\pi^*/^3\pi\pi^*$	14/0	-135/16	-3/0	27/-3	11/0	-108/13	109/13
	$^1n\pi^*/^3n\pi^*$	0/0	0/0	0/0	0/0	0/0	0/0	0/0
GMC-QDPT2//PBE0	GS/$^3\pi\pi^*$	0/0	1/-1	0/0	0/0	0/0	1/-1	1/1
	GS/$^3n\pi^*$	-14/0	123/16	3/0	-26/-3	-11/0	97/13	98/13
	$^1n\pi^*/^3\pi\pi^*$	-14/0	-140/17	3/0	28/-3	-11/0	-112/14	113/14
	$^1n\pi^*/^3n\pi^*$	0/0	1/0	0/0	0/0	0/0	1/0	1/0
MRSF/B3LYP	GS/$^3\pi\pi^*$	0/0	-1/-1	0/0	0/1	0/0	-1/0	1/0
	GS/$^3n\pi^*$	-15/0	100/-10	4/0	-20/2	-11/0	80/-8	81/8
	$^1n\pi^*/^3\pi\pi^*$	12/0	-137/16	-3/0	27/-3	9/0	-110/13	110/13
	$^1n\pi^*/^3n\pi^*$	0/0	0/0	0/0	0/0	0/0	0/0	0/0
GMC-QDPT2//B3LYP	GS/$^3\pi\pi^*$	0/0	-1/-1	0/0	0/0	0/0	-1/-1	1/1
	GS/$^3n\pi^*$	-16/0	133/16	3/0	-26/-3	-13/0	107/13	108/13
	$^1n\pi^*/^3\pi\pi^*$	16/0	140/17	-3/0	-28/-3	13/0	112/14	113/14
	$^1n\pi^*/^3n\pi^*$	0/0	1/0	0/0	0/0	0/0	1/0	1/0
MRSF/BH&HLYP	GS/$^3\pi\pi^*$	0/0	0/0	0/0	0/0	0/0	0/0	0/0
	GS/$^3n\pi^*$	20/0	-120/12	-5/0	24/-2	16/0	-96/10	97/10
	$^1n\pi^*/^3\pi\pi^*$	21/0	-143/16	-4/0	28/-3	17/0	-115/13	116/13
	$^1n\pi^*/^3n\pi^*$	0/0	1/0	0/0	0/0	0/0	1/0	1/0
GMC-QDPT2//BH&HLYP	GS/$^3\pi\pi^*$	0/0	2/-1	0/0	-1/0	0/0	1/-1	1/1
	GS/$^3n\pi^*$	-18/0	133/15	4/0	-26/-3	-14/0	107/12	108/12
	$^1n\pi^*/^3\pi\pi^*$	18/0	143/-16	-4/0	-28/3	14/0	115/-13	116/13
	$^1n\pi^*/^3n\pi^*$	0/0	-2/0	0/0	0/0	0/0	-2/0	2/0
MRSF/M06-2X	GS/$^3\pi\pi^*$	5/0	3/-3	0/0	-1/1	5/0	2/-2	5/2
	GS/$^3n\pi*$	-18/0	124/-12	4/0	-25/2	-14/0	99/-10	100/10
	$^1n\pi^*/^3\pi\pi^*$	-16/0	133/-6	3/0	-26/1	13/0	107/-5	108/5
	$^1n\pi^*/^3n\pi^*$	0/0	2/0	0/0	0/0	0/0	2/0	2/0
GMC-QDPT2//M06-2X	GS/$^3\pi\pi^*$	4/0	-3/-2	0/0	1/1	4/0	-2/-1	4/1
	GS/$^3n\pi^*$	-19/0	142/19	4/0	-28/-4	-15/0	114/15	115/15
	$^1n\pi^*/^3\pi\pi^*$	17/0	147/-13	-3/0	-29/3	14/0	118/-10	119/10
	$^1n\pi^*/^3n\pi^*$	0/0	3/0	0/0	-1/0	0/0	2/0	2/0

in Fig. 4 along with the major configurations of GS, S_1, T_1 and 2_2 states. It is seen that the n_S and π orbitals are mainly composed of S nonbonding and π orbitals, which is the main source of large SOC values.

Intersystem Crossing of Thymine

The controversy over the relaxation mechanism of photoexcited thymine such as S_1-trapping, S_2-trapping, and S_1&S_2-trapping has been recently resolved by our NAMD study using MRSF-TDDFT.[22] Our study supports the S_1-trapping mechanism with two lifetimes, τ_1=30$\pm$1 fs and τ_2=6.1$\pm$0.035 ps, quantitatively consistent with the recent time-resolved experiments.[2] Accordingly, upon photo-excitation to the S_2 ($\pi\pi^*$) state, thymine undergoes an ultrafast (*ca.* 30 fs) $S_2 \rightarrow S_1$ internal conversion through (IC) a conical intersection ($CI_{21,BLA}$) and resides around the minimum on the S_{1min} ($n_O\pi^*$) surface, slowly decaying to the ground state (*ca.* 6.1 ps). Therefore, it is clear that the S_{1min} is the most frequently sampled structure during the overall lifetime of thymine. Apart from the singlet state models, some computations[61,62] suggested a possibility of the $^1n\pi^* \rightarrow {}^3\pi\pi^*$ ($S_1 \rightarrow T_2$) intersystem crossing (ISC). For example, the CASSCF NAMD simulations of Mai et al.[62] predicted a 0.9$\pm$0.1 ps time scale for the $S_1 \rightarrow T_2$ intersystem crossing (ISC) followed by an ultrafast relaxation to T_1. As discussed in the introduction, Wolf et al.[2] have obtained circumstantial experimental evidence of the population transfer to triplet states on the timescale of 3.5$\pm$0.3 ps.

In addition to the bright S_2 ($\pi\pi^*$) and dark S_1 ($n\pi^*$), the energies of T_3 ($\pi\pi^*$), T_2 ($n\pi^*$) and T_1 ($\pi\pi^*$) are calculated along the bond-length alternation (BLA) coordinate of the molecular backbone, which connects the FC (Franck-Condon) geometry with S_{1min} via IC, and the results are shown in the Figure 5a. It is clearly seen that the T_2 is nearly parallel with S_1 from FC to S_{1min}, with a negligibly small T_2-S_1 energy gap. This is because the n and π^* orbitals in the two $n\pi^*$ states point along different directions (in-plane vs. out-of-plane) and hence give a small exchange integral, which determines the gap between the singlet and triplet states of the $n\pi^*$ configuration. According to El-Sayed's rule, the same-configuration-intersystem crossing from S_1 ($n\pi^*$) to T_2

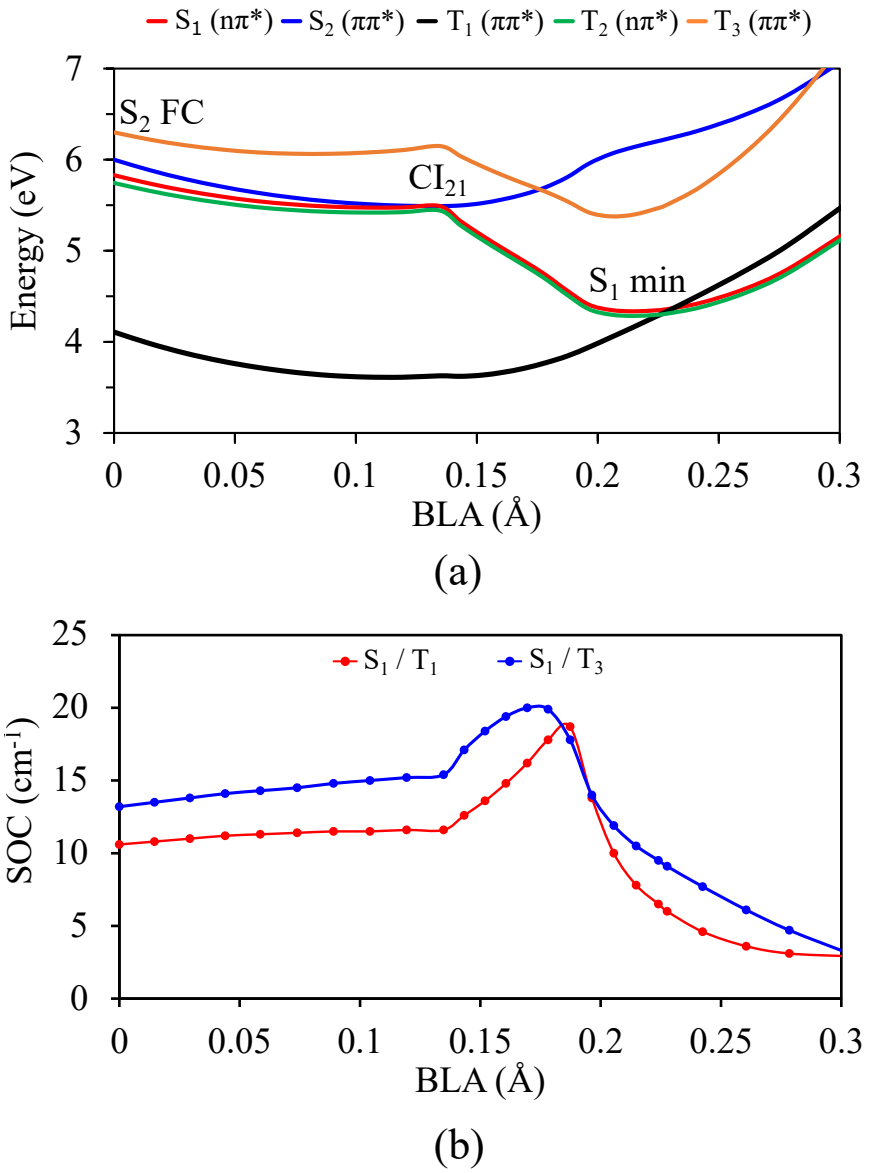

Figure 5: (a) Minimum energy paths (MEPs) using the NEB method[59,60] connecting the FC region, the $\mathrm{CI}_{21,BLA}$, and the S_{1min} geometries obtained by MRSF/BH&HLYP/6-31G* from Ref. 22. The BLA coordinate is defined here as the difference between the average increments of the lengths of the double bonds and the decrease of the single bond, $\mathrm{BLA} = \frac{1}{2}(\Delta R_{\mathrm{C_4{=}O_8}} + \Delta R_{\mathrm{C_5{=}C_6}}) - \Delta R_{\mathrm{C_4{-}C_5}}$, where ΔR's are displacements with respect to the S_0 equilibrium geometry. (b) The SOC values between $M_s = 0$ singlet and $M_s = \pm 1$ triplet states.

($n\pi^*$) is inefficient, even though their energies are nearly identical in the entire region of PES. Remarkably, however, the more stable T_1 ($\pi\pi^*$ the thick black curve) crosses with S_1 and T_2

near S_{1min}, providing a plausible route of IC or ISC. Thus, the most probable initial intersystem crossing (IRC) would be $S_1 \rightarrow T_1$ or $S_1 \rightarrow T_3$ pathways. While T_1 has a crossing with S_1 at S_{1min} structure, the T_3 is ~ 1 eV higher than S_1 along the entire PES. Therefore, the former ISC is more likely to occur. The corresponding SOC values are presented in Fig. 5b. In terms of S_1/T_1 SOC magnitude, the initial values at FC (10.4 cm^{-1}) is increased to 19 cm^{-1} at BLA=0.19. It is quite significantly decreased afterward to 3 cm^{-1}. The same trend can be seen from the SOC values of S_1/T_3 ($M_s = \pm 1$) curve.

To further analyze the ISC, the reference RO-DFT orbitals at the three different geometries of FC, $CI_{21,BLA}$ and S_{1min} are presented in Fig. 6 along with the contributions of each transitions in the parenthesis. It turned out that not only n, π and π^* MOs but also $n^{'}$, $\pi^{'}$ and $\pi^{'*}$ MOs are involved in the major transitions of S_1, T_1 and T_3 states. At the FC structure, the characters of S_1, S_2, T_1, T_2 and T_3 states may be denoted as $n\pi^*$, $\pi\pi^*$, $\pi\pi^*$, $n\pi^*$ and $\pi\pi^*$, respectively. The orbital energy of n at FC is reduced from -9.10 to -9.25 ($CI_{21,BLA}$) and -10.40 eV (S_{1min}), which explains well the stability of S_1 and T_2. Although the T_1 has an entirely $\pi\pi^*$ character, however, the π orbital at FC and CI_{21} is mostly composed of C=C π bonding, while that at $S_{1,min}$ is located on oxygen. The character of T_3 is the combination of $\pi^{'}\pi^*$ and $\pi\pi^{'*}$, utilizing the two different oxygen π orbitals. As the BLA increases such as $S_{1,min}$ structure, the contribution of the former character increases. The lowest singlet excited state S_1 is mostly composed of $n\pi^*$ with a minor $n^{'}\pi^*$ at FC. However, the latter character dominates at $S_{1,min}$. Therefore, the significantly decreased SOC values of both S_1/T_1 and S_1/T_3 at $S_{1,min}$ can be attributed to character changes. For example, the SOC between $n^{'}$(S_1) and $\pi^{'}$ (T_3) can be small due to the small overlap between the corresponding orbitals.

If the $S_1 \longrightarrow T_1$ ISC takes place, the T_1 population would eventually reside at a structure near BLA=0.12 , since it corresponds to the T_1 minimum. As the majority of excited state populations stay at the vicinity of S_{1min} [22] and the S_1-T_1 crossing is at the proximity of the S_1 minimum, even if the SOC between T_1 and S_1 near S_{1min} is small ~ 3 cm^{-1}, there is a chance for the S_1 to T_1 ISC due to frequent sampling of the S_1-T_1 crossing region during excited state dynamics.

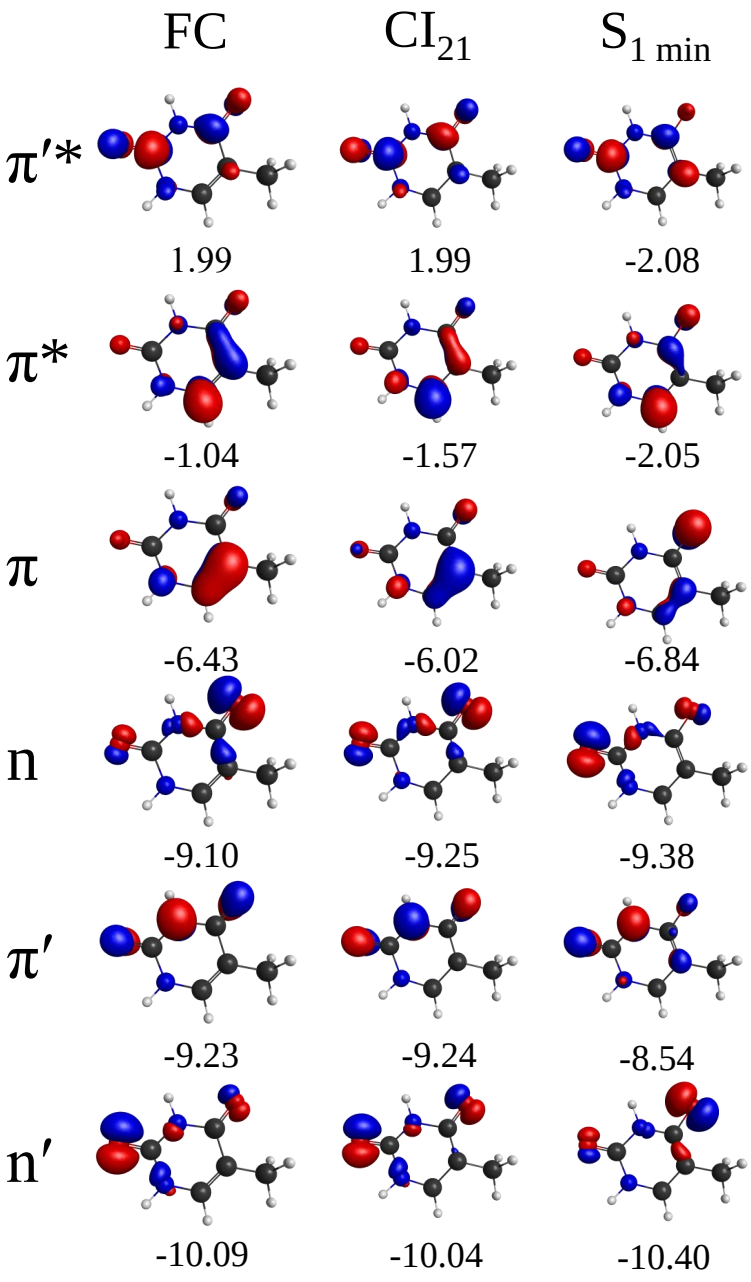

Figure 6: RO-DFT/BH&HLYP/6-31G* molecular orbitals of thymine and their energies in eV. The character of S_1, T_1, and T_3 states with squared transition coefficients are given in bottom.

Conclusions

A relativistic MRSF-TDDFT (SOC-MRSF for brevity) protocol has been developed, where the spin-dependent Hamiltonian contains the explicit spin-orbit coupling (SOC) operator in a perturbative manner. The relativistic spin-orbit coupled (SOC) states are represented as a linear combination of non-SOC states. The matrix elements of SOC Hamiltonian consist of both one- and two-electron contributions. The latter is treated by a mean-field screening approximation.

The resulting SOC-MRSF reproduces the experimental values with very high accuracy, which are comparable to the fully relativistic four-component (4c) CASSCF and 4c-CASPT2 in the calculations of the $^3P_0 -^3 P_1$ gaps of the C, Si and Ge atoms. The particular combination of BH&HLYP/cc-pVTZ produces near-perfect agreements with experimental values. Even in the case of fifth-row element Sn with its strong SOC, a remarkable accuracy ($\sim$ 3 $\%$ error) was achieved. The SOC couplings of C and Si have also been predicted within $\sim$ 10 $\%$ error. In the SOC calculation of 4-thiothymine, the values by SOC-MRSF are in excellent agreement with the reference values by GMC-QDPT2, regardless of exchange-correlation functionals. The possibility of ISC in thymine was also investigated. It was found that the T_1 ($\pi\pi^*$) crosses with S_1 and T_2 near S_{1min}, providing a good chance of IC or ISC. In the case of S_1/T_1, non-zero SOC magnitude at the crossing position can allow S_1 ($n\pi^*$) $\longrightarrow$ T_1 ($\pi\pi^*$) ISC. It can be expected that if the majority of excited state populations are staying near S_{1min}, the chance of ISC may increase due to the proximity between the S_1/T_1 crossing and S_{1min}.

In short, current results established that SOC-MRSF is not only accurate but also practical as compared to highly correlated but computation-intensive theories. Accordingly, SOC-MRSF can be a promising protocol for SOC-involved nonadiabatic molecular dynamics (NAMD), especially for large molecules.

Acknowledgements

This work was supported by the NRF funded by the Ministry of Science and ICT (2020R1A2C2008246 and 2020R1A5A1019141) and by the Samsung Advanced Institute of Technology (IO211126-09177-01) This work was also supported by the Korea Polar Research Institute(KOPRI, PE22120) funded by the Ministry of Oceans and Fisheries. T.Z. thanks the Natural Sciences and Engineering Research Council (NSERC) of Canada for research funding (RGPIN-2016-06276) and York University for start-up grant (481333). T.Z. also thanks Compute Canada and Digital Research Alliance of Canada for computational resources. Work by S.L. was funded by the US Department of Energy, Office of Science, via Award DE-SC0019374.

References

(1) Alías-Rodríguez, M.; De Graaf, C.; Huix-Rotllant, M. Ultrafast Intersystem Crossing in Xanthone from Wavepacket Dynamics. *J. Am. Chem. Soc.* **2021**, *143*, 21474–21477.

(2) Wolf, T. J. A.; Parrish, R. M.; Myhre, R. H.; Martinez, T. J.; Koch, H.; Gühr, M. Observation of Ultrafast Intersystem Crossing in Thymine by Extreme Ultraviolet Time-Resolved Photoelectron Spectroscopy. *J. Phys. Chem. A* **2019**, *123*, 6897–6903.

(3) Mukherjee, S.; Fedorov, D. A.; Varganov, S. A. Modeling spin-crossover dynamics. *Annu. Rev. Phys. Chem.* **2021**, *72*.

(4) Marian, C. M. Spin–orbit coupling and intersystem crossing in molecules. *Wiley Interdiscip. Rev. Comput. Mol. Sci.* **2012**, *2*, 187–203.

(5) Cunha, L. A.; Hait, D.; Kang, R.; Mao, Y.; Head-Gordon, M. Relativistic Orbital-Optimized Density Functional Theory for Accurate Core-Level Spectroscopy. *J. Phys. Chem. Lett* **2022**, *13*, 3438–3449.

(6) Endo, A.; Ogasawara, M.; Takahashi, A.; Yokoyama, D.; Kato, Y.; Adachi, C. Thermally

activated delayed fluorescence from Sn4+–porphyrin complexes and their application to organic light emitting diodes—A novel mechanism for electroluminescence. *Advanced Materials* **2009**, *21*, 4802–4806.

(7) Casida, M. E.; Huix-Rotllant, M. Progress in time-dependent density-functional theory. *Annu. Rev. Phys. Chem.* **2012**, *63*, 287–323.

(8) Lee, S.; Shostak, S.; Filatov, M.; Choi, C. H. Conical Intersections in Organic Molecules: Benchmarking Mixed-Reference Spin–Flip Time-Dependent DFT (MRSF-TD-DFT) vs Spin–Flip TD-DFT. *J. Phys. Chem. A* **2019**, *123*, 6455–6462.

(9) Park, W.; Shen, J.; Lee, S.; Piecuch, P.; Filatov, M.; Choi, C. H. Internal Conversion between Bright (11 B u+) and Dark (21 A g–) States in s-trans-Butadiene and s-trans-Hexatriene. *J. Phys. Chem. Lett.* **2021**, *12*, 9720–9729.

(10) Lee, S.; Filatov, M.; Lee, S.; Choi, C. H. Eliminating spin-contamination of spin-flip time dependent density functional theory within linear response formalism by the use of zeroth-order mixed-reference (MR) reduced density matrix. *J. Chem. Phys.* **2018**, *149*, 104101.

(11) Lee, S.; Kim, E. E.; Nakata, H.; Lee, S.; Choi, C. H. Efficient implementations of analytic energy gradient for mixed-reference spin-flip time-dependent density functional theory (MRSF-TDDFT). *J. Chem. Phys.* **2019**, *150*, 184111.

(12) Lee, S.; Park, W.; Nakata, H.; Filatov, M.; Choi, C. H. Recent advances in ensemble density functional theory and linear response theory for strong correlation. *Bull. Korean Chem. Soc.* **2022**, *43*, 17–34.

(13) Shao, Y.; Head-Gordon, M.; Krylov, A. I. The spin–flip approach within time-dependent density functional theory: Theory and applications to diradicals. *J. Chem. Phys.* **2003**, *118*, 4807–4818.

(14) Horbatenko, Y.; Sadiq, S.; Lee, S.; Filatov, M.; Choi, C. H. Mixed-Reference Spin-Flip Time-Dependent Density Functional Theory (MRSF-TDDFT) as a Simple yet Accurate Method for Diradicals and Diradicaloids. *J. Chem. Theory Comput.* **2021**, *17*, 848–859.

(15) Lee, S.; Kim, E.; Lee, S.; Choi, C. H. Fast Overlap Evaluations for Nonadiabatic Molecular Dynamics Simulations: Applications to SF-TDDFT and TDDFT. *J. Chem. Theory Comput.* **2019**, *15*, 882.

(16) Horbatenko, Y.; Lee, S.; Filatov, M.; Choi, C. H. Performance Analysis and Optimization of Mixed-Reference Spin-Flip Time-Dependent Density Functional Theory (MRSF-TDDFT) for Vertical Excitation Energies and Singlet–Triplet Energy Gaps. *J. Phys. Chem. A* **2019**, *123*, 7991.

(17) Lee, S.; Horbatenko, Y.; Filatov, M.; Choi, C. H. Fast and Accurate Computation of Nonadiabatic Coupling Matrix Elements Using the Truncated Leibniz Formula and Mixed-Reference Spin-Flip Time-Dependent Density Functional Theory. *J. Phys. Chem. Lett.* **2021**, *12*, 4722–4728.

(18) Baek, Y. S.; Lee, S.; Filatov, M.; Choi, C. H. Optimization of Three State Conical Intersections by Adaptive Penalty Function Algorithm in Connection with the Mixed-Reference Spin-Flip Time-Dependent Density Functional Theory Method (MRSF-TDDFT). *J. Phys. Chem. A* **2021**, *125*, 1994–2006.

(19) Pomogaev, V.; Lee, S.; Shaik, S.; Filatov, M.; Choi, C. H. Exploring Dyson's Orbitals and Their Electron Binding Energies for Conceptualizing Excited States from Response Methodology. *J. Phys. Chem. Lett.* **2021**, *12*, 9963–9972.

(20) Horbatenko, Y.; Lee, S.; Filatov, M.; Choi, C. H. How Beneficial Is the Explicit Account of Doubly-Excited Configurations in Linear Response Theory? *J. Chem. Theory Comput.* **2021**, *17*, 975–984.

(21) Kim, H.; Park, W.; Kim, Y.; Filatov, M.; Choi, C. H.; Lee, D. Relief of excited-state antiaromaticity enables the smallest red emitter. *Nat. Commun.* **2021**, *12*, 1–9.

(22) Park, W.; Lee, S.; Huix-Rotllant, M.; Filatov, M.; Choi, C. H. Impact of the Dynamic Electron Correlation on the Unusually Long Excited-State Lifetime of Thymine. *J. Phys. Chem. Lett.* **2021**, *12*, 4339–4346.

(23) Park, W.; Shen, J.; Lee, S.; Piecuch, P.; Joo, T.; Filatov, M.; Choi, C. H. Dual Fluorescence of Octatetraene Hints at a Novel Type of Singlet-to-Singlet Thermally Activated Delayed Fluorescence Process. *J. Phys. Chem. C* **2022**,

(24) Park, W.; Filatov, M.; Sadiq, S.; Gerasimov, I.; Lee, S.; Joo, T.; Choi, C. H. A Plausible Mechanism of Uracil Photohydration Involves an Unusual Intermediate. *J. Phys. Chem. Lett.* **2022**, *13*, 7072–7080.

(25) Japahuge, A.; Lee, S.; Choi, C. H.; Zeng, T. Design of singlet fission chromophores with cyclic (alkyl)(amino) carbene building blocks. *J. Chem. Phys.* **2019**, *150*, 234306.

(26) Pradhan, E.; Lee, S.; Choi, C. H.; Zeng, T. Diboron-and diaza-doped anthracenes and phenanthrenes: their electronic structures for being singlet fission chromophores. *J. Phys. Chem. A* **2020**, *124*, 8159–8172.

(27) James, D.; Pradhan, E.; Lee, S.; Choi, C. H.; Zeng, T. Dicarbonyl anthracenes and phenanthrenes as singlet fission chromophores. *Can. J. Chem.* **2022**, *99*, 1–10.

(28) Konecny, L.; Repisky, M.; Ruud, K.; Komorovsky, S. Relativistic four-component linear damped response TDDFT for electronic absorption and circular dichroism calculations. *J. Chem. Phys.* **2019**, *151*, 194112.

(29) Gao, J.; Liu, W.; Song, B.; Liu, C. Time-dependent four-component relativistic density functional theory for excitation energies. *J. Chem. Phys.* **2004**, *121*, 6658–6666.

(30) Gao, J.; Zou, W.; Liu, W.; Xiao, Y.; Peng, D.; Song, B.; Liu, C. Time-dependent four-component relativistic density-functional theory for excitation energies. II. The exchange-correlation kernel. *J. Chem. Phys.* **2005**, *123*, 054102.

(31) Casida, M. E. *Recent Advances In Density Functional Methods: (Part I)*; World Sci., 1995; pp 155–192.

(32) Marian, C. WIREs: Comput. *Mol. Sci* **2012**, *2*, 187–203.

(33) Heß, B. A.; Marian, C. M.; Wahlgren, U.; Gropen, O. A mean-field spin-orbit method applicable to correlated wavefunctions. *Chemical Physics Letters* **1996**, *251*, 365–371.

(34) Neuscamman, E.; Yanai, T.; Chan, G. K.-L. Quadratic canonical transformation theory and higher order density matrices. *J. Chem. Phys.* **2009**, *130*, 124102.

(35) Saitow, M.; Kurashige, Y.; Yanai, T. Multireference configuration interaction theory using cumulant reconstruction with internal contraction of density matrix renormalization group wave function. *J. Chem. Phys.* **2013**, *139*, 044118.

(36) Wick, G.-C. The evaluation of the collision matrix. *Phys. Rev.* **1950**, *80*, 268.

(37) Zhang, B.; Vandezande, J. E.; Reynolds, R. D.; Schaefer, H. F. Spin-Orbit Coupling via Four-Component Multireference Methods: Benchmarking on p-Block Elements and Tentative Recommendations. *J. Chem. Theory Comput.* **2018**, *14*, 1235–1246.

(38) Haris, K.; Kramida, A. Critically Evaluated Spectral Data for Neutral Carbon (). *Astrophys. J., Suppl. Ser.* **2017**, *233*, 16.

(39) Martin, W. C.; Zalubas, R. Energy levels of silicon, Si I through Si XIV. *J. Phys. Chem. Ref. Data* **1983**, *12*, 323–380.

(40) Sugar, J.; Musgrove, A. Energy levels of germanium, Ge I through Ge XXXII. *J. Phys. Chem. Ref. Data* **1993**, *22*, 1213–1278.

(41) Oliver, P.; Hibbert, A. Energy level classifications and Breit–Pauli oscillator strengths in neutral tin. *J. Phys. B: At. Mol. Opt. Phys* **2008**, *41*, 165003.

(42) Huix-Rotllant, M.; Natarajan, B.; Ipatov, A.; Wawire, C. M.; Deutsch, T.; Casida, M. E. Assessment of noncollinear spin-flip Tamm–Dancoff approximation time-dependent density-functional theory for the photochemical ring-opening of oxirane. *Phys. Chem. Chem. Phys.* **2010**, *12*, 12811–12825.

(43) Fedorov, D. G.; Koseki, S.; Schmidt, M. W.; Gordon, M. S. Spin-orbit coupling in molecules: Chemistry beyond the adiabatic approximation. *Int. Rev. Phys. Chem* **2003**, *22*, 551–592.

(44) Koseki, S.; Schmidt, M. W.; Gordon, M. S. Effective nuclear charges for the first-through third-row transition metal elements in spin- orbit calculations. *The Journal of Physical Chemistry A* **1998**, *102*, 10430–10435.

(45) Koseki, S.; Fedorov, D. G.; Schmidt, M. W.; Gordon, M. S. Spin- Orbit Splittings in the Third-Row Transition Elements: Comparison of Effective Nuclear Charge and Full Breit-Pauli Calculations. *The Journal of Physical Chemistry A* **2001**, *105*, 8262–8268.

(46) Barysz, M.; Sadlej, A. J. Two-component methods of relativistic quantum chemistry: from the Douglas–Kroll approximation to the exact two-component formalism. *J. Mol. Struct.: THEOCHEM* **2001**, *573*, 181–200.

(47) Barysz, M. The relativistic scheme for eliminating small components Hamiltonian: Analysis of approximations. *J. Chem. Phys.* **2000**, *113*, 4003–4007.

(48) Berning, A.; Schweizer, M.; Werner, H.-J.; Knowles, P. J.; Palmieri, P. Spin-orbit matrix elements for internally contracted multireference configuration interaction wavefunctions. *Mol. Phys.* **2000**, *98*, 1823–1833.

(49) Bethe, H. A.; Salpeter, E. E. *Quantum mechanics of one-and two-electron atoms*; Springer Science & Business Media, 2012.

(50) Bai, S.; Barbatti, M. Why replacing different oxygens of thymine with sulfur causes distinct absorption and intersystem crossing. *J. Phys. Chem. A* **2016**, *120*, 6342–6350.

(51) Reichardt, C.; Crespo-Hernández, C. E. Room-temperature phosphorescence of the DNA monomer analogue 4-thiothymidine in aqueous solutions after UVA excitation. *J. Phys. Chem. Lett.* **2010**, *1*, 2239–2243.

(52) Perun, S.; Sobolewski, A. L.; Domcke, W. Conical intersections in thymine. *J. Phys. Chem. A* **2006**, *110*, 13238–13244.

(53) Pirillo, J.; De Simone, B. C.; Russo, N. Photophysical properties prediction of selenium-and tellurium-substituted thymidine as potential UVA chemotherapeutic agents. *Theoretical Chemistry Accounts* **2016**, *135*, 1–5.

(54) Cui, G.; Thiel, W. Intersystem crossing enables 4-thiothymidine to act as a photosensitizer in photodynamic therapy: an ab initio QM/MM study. *J. Phys. Chem. Lett.* **2014**, *5*, 2682–2687.

(55) Harada, Y.; Okabe, C.; Kobayashi, T.; Suzuki, T.; Ichimura, T.; Nishi, N.; Xu, Y.-Z. Ultrafast intersystem crossing of 4-thiothymidine in aqueous solution. *J. Phys. Chem. Lett.* **2010**, *1*, 480–484.

(56) Pollum, M.; Jockusch, S.; Crespo-Hernandez, C. E. 2, 4-Dithiothymine as a potent UVA chemotherapeutic agent. *J. Am. Chem. Soc.* **2014**, *136*, 17930–17933.

(57) Gao, X.; Bai, S.; Fazzi, D.; Niehaus, T.; Barbatti, M.; Thiel, W. Evaluation of Spin-Orbit Couplings with Linear-Response Time-Dependent Density Functional Methods. *Journal of Chemical Theory and Computation* **2017**, *13*, 515–524.

(58) Nakano, H.; Uchiyama, R.; Hirao, K. Quasi-degenerate perturbation theory with general multiconfiguration self-consistent field reference functions. *Journal of computational chemistry* **2002**, *23*, 1166–1175.

(59) Jónsson, H.; Mills, G.; Jacobsen, K. W. In *Classical and Quantum Dynamics in Condensed Phase Simulations*; Berne, B. J., Ciccotti, G., Coker, D. F., Eds.; World Sci.: Singapore, 1998; Chapter 16, pp 385–404.

(60) Kästner, J.; Carr, J. M.; Keal, T. W.; Thiel, W.; Wander, A.; Sherwood, P. DL-FIND: an open-source geometry optimizer for atomistic simulations. *J. Phys. Chem. A* **2009**, *113*, 11856–11865.

(61) Serrano-Pérez, J. J.; González-Luque, R.; Merchán, M.; Serrano-Andrés, L. On the Intrinsic Population of the Lowest Triplet State of Thymine. *J. Phys. Chem. B* **2007**, *111*, 11880–11883.

(62) Mai, S.; Richter, M.; Marquetand, P.; González, L. The DNA nucleobase thymine in motion - Intersystem crossing simulated with surface hopping. *Chemi. Phys.* **2017**, *482*, 9–15.